



Cite this: *Phys. Chem. Chem. Phys.*,  
2024, 26, 14046

# Interface design of SARS-CoV-2 symmetrical nsp7 dimer and machine learning-guided nsp7 sequence prediction reveals physicochemical properties and hotspots for nsp7 stability, adaptation, and therapeutic design†

Amar Jeet Yadav,  Shivank Kumar,  Shweeta Maurya,  Khushboo Bhagat   
and Aditya K. Padhi \*

The COVID-19 pandemic, driven by severe acute respiratory syndrome coronavirus 2 (SARS-CoV-2), necessitates a profound understanding of the virus and its lifecycle. As an RNA virus with high mutation rates, SARS-CoV-2 exhibits genetic variability leading to the emergence of variants with potential implications. Among its key proteins, the RNA-dependent RNA polymerase (RdRp) is pivotal for viral replication. Notably, RdRp forms dimers *via* non-structural protein (nsp) subunits, particularly nsp7, crucial for efficient viral RNA copying. Similar to the main protease (M<sup>Pro</sup>) of SARS-CoV-2, there is a possibility that the nsp7 might also undergo mutational selection events to generate more stable and adaptable versions of nsp7 dimer during virus evolution. However, efforts to obtain such cohesive and comprehensive information are lacking. To address this, we performed this study focused on deciphering the molecular intricacies of nsp7 dimerization using a multifaceted approach. Leveraging computational protein design (CPD), machine learning (ML), AlphaFold v2.0-based structural analysis, and several related computational approaches, we aimed to identify critical residues and mutations influencing nsp7 dimer stability and adaptation. Our methodology involved identifying potential hotspot residues within the dimeric nsp7 interface using an interface-based CPD approach. Through Rosetta-based symmetrical protein design, we designed and modulated nsp7 dimerization, considering selected interface residues. Analysis of physicochemical features revealed acceptable structural changes and several structural and residue-specific insights emphasizing the intricate nature of such protein–protein complexes. Our ML models, particularly the random forest regressor (RFR), accurately predicted binding affinities and ML-guided sequence predictions corroborated CPD findings, elucidating potential nsp7 mutations and their impact on binding affinity. Validation against clinical sequencing data demonstrated the predictive accuracy of our approach. Moreover, AlphaFold v2.0 structural analyses validated optimal dimeric configurations of affinity-enhancing designs, affirming methodological precision. Affinity-enhancing designs exhibited favourable energetics and higher binding affinity as compared to their counterparts. The obtained physicochemical properties, molecular interactions, and sequence predictions advance our understanding of SARS-CoV-2 evolution and inform potential avenues for therapeutic intervention against COVID-19.

Received 7th March 2024,  
Accepted 15th April 2024

DOI: 10.1039/d4cp01014k

rs.c.li/pccp

## Introduction

The ongoing COVID-19 pandemic, caused by SARS-CoV-2, has posed an exemplary worldwide dilemma, demanding a

comprehensive understanding of the virus, its components, and its life cycle for effective prevention and control.<sup>1,2</sup> SARS-CoV-2, belonging to the Coronaviridae family, is an enveloped, positive-sense, single-stranded RNA virus with the largest genome among known RNA viruses.<sup>3</sup> The genome of SARS-CoV-2 is approximately 30 kilobases in length and encodes numerous proteins involved in viral replication, transcription, host interaction, and immune evasion.<sup>4</sup> Key structural proteins include spike (S), envelope (E), membrane (M), and nucleocapsid (N) proteins.<sup>5</sup> Several non-structural proteins also play key roles in

Laboratory for Computational Biology & Biomolecular Design, School of Biochemical Engineering, Indian Institute of Technology (BHU), Varanasi 221005, Uttar Pradesh, India. E-mail: [aditya.bce@iitbhu.ac.in](mailto:aditya.bce@iitbhu.ac.in),  
Web: <https://www.iitbhu.ac.in/dept/bce/people/adityabce>

† Electronic supplementary information (ESI) available. See DOI: <https://doi.org/10.1039/d4cp01014k>

regulating the immune system and viral replication.<sup>6</sup> In addition to the structural components, non-structural proteins, and accessory proteins, SARS-CoV-2 has a positive-sense, single-stranded RNA genome, making it unique among coronaviruses.<sup>7</sup>

SARS-CoV-2, like all RNA viruses, exhibits genetic variability due to its high mutation rate.<sup>8</sup> This genetic diversity has given rise to various SARS-CoV-2 lineages and variants, some of which have garnered substantial attention due to their potential impact on transmissibility, severity, vaccine effectiveness, and diagnostic accuracy.<sup>9</sup> Variants such as alpha, beta, gamma, delta, omicron and recently identified sub-variants like JN.1 have specific mutations in the spike protein and other regions of the genome, which have raised concerns about their ability to evade immunity, influence viral replication, and alter the course of the pandemic.<sup>10</sup> These variants mostly emerged from mutations in the intracellular proteins of SARS-CoV-2, and to fully grasp the impact of these variants, it is crucial to investigate the molecular mechanisms that underpin viral replication, immune evasion, and pathogenesis.<sup>11</sup> This examination is particularly relevant for intracellular proteins, as they play a pivotal role in the lifecycle of the virus and its interactions with host cells.<sup>12,13</sup>

Among the intracellular proteins, RdRp is a key player in the viral life cycle, which serves as the primary enzyme responsible for replicating the viral genome.<sup>14</sup> It catalyzes the formation of negative-sense RNA strands from positive-sense RNA templates, a critical step in viral replication.<sup>15</sup> The high fidelity and activity of RdRp are critical for ensuring viral genome integrity and efficient replication.<sup>16</sup> The molecular intricacies of RdRp and the dimerization of non-structural protein (nsp) subunits hold the key to deciphering viral replication mechanisms and exploring therapeutic interventions.<sup>17</sup> One of the intriguing aspects of RdRp is its ability to form dimers (*via* its nsp7 subunits), which is essential for its functionality in SARS-CoV-2.<sup>18</sup> RdRp dimerization is a complex and tightly regulated process that involves interactions with nsp subunits, particularly nsp7 and nsp8.<sup>19</sup> The dimeric RdRp, in its antiparallel arrangement, plays a crucial role in governing the processivity of the enzyme and efficiency in copying the viral RNA.<sup>20</sup> While much research has focused on RdRp as an individual entity and targeting it, the molecular mechanisms and structural basis of RdRp dimerization, specifically the nsp subunits, are an emerging area of interest, holding the potential to unveil new antiviral strategies and therapeutic targets.<sup>14</sup>

In our recent studies, we harnessed the power of high-throughput protein design methodologies to pinpoint critical residues and mutations within intracellular proteins including main protease ( $M^{pro}$ ), RdRp, and spike protein receptor binding domain (RBD) of SARS-CoV-2, which could make the virus more tolerant and adaptable to antiviral drugs such as remdesivir, molnupiravir, favipiravir, nirmatrelvir and bebtelovimab.<sup>21–26</sup> While conducting this research, we found that mutational and residue-specific changes can induce relative stabilities and adaptability of the RdRp, for instance, the nsp7 by forming symmetrical dimers.<sup>20</sup> This realization prompted us to perform

an extensive protein design and ML-based endeavour, which was further complemented by a comprehensive multi-parametric analysis.<sup>27</sup> To obtain these insights for the dimeric RdRp formed *via* the nsp7 subunits, we employed a unique protein design approach, followed by evaluation of various physicochemical features, comparative analysis against clinical sequencing data, ML-guided binding affinity, and nsp7 sequence prediction, and rigorous structural validation through the utilization of AlphaFold v2.0.<sup>28</sup> This concerted effort led us to discern the specific hotspot residues within the dimeric RdRp of the virus that display a heightened proclivity towards stability, adaptation, and improved fitness.<sup>20</sup>

## Materials and methods

### Identification of interface residues in nsp7

The electron microscopic structure of the dimeric form of SARS-CoV-2 RdRp in complex with nsp7:nsp8:nsp12:primer dsRNA (PDB ID: 7OYG) was utilized to obtain detailed information on nsp7–nsp7 dimerization and its interface residues. The RdRp dimer structure in its antiparallel arrangement, possesses one copy of nsp8 each and dimerizes *via* the nsp7 subunits.<sup>20</sup> This analysis identified 30 nsp7 residues that are part of the dimeric interface and helped in its dimerization. Following this, the structure was used for the interface-based symmetrical protein design.

### Interface-based symmetrical dimer design of nsp7

The structure was first energy-minimized and refined using Rosetta's relax protocol. Multiple structures were generated during this step to identify the lowest-energy structure. A symmetry definition file was created using the lowest-energy dimeric structure of nsp7. The relaxed structure was then used as an input for designing the nsp7 interface residues involved in the dimerization of nsp7.<sup>29–31</sup> Incorporating backbone flexibility, the Rosetta macromolecular modeling suite was applied to redesign the interface residues of the nsp7 dimer. In this step, the 30 interfacial residues of nsp7 dimer were designed with selected single nucleotide polymorphisms (SNPs).<sup>32</sup> A modified Rosetta script with backbone flexibility of nsp7 was considered while designing in addition to the Monte-Carlo simulated annealing and the Rosetta all-atom force field model. The dimeric interface of nsp7 residues was studied for potential hotspots that could change to allow for a stronger and more stable nsp7 dimer and their adaptation. From the design experiment, a total of 100 000 dimeric designs of nsp7 were generated. The Rosetta total score, root mean square deviation (RMSD), Rosetta interface  $\Delta\Delta G$  (illustrating the binding affinities between the two designed symmetrical nsp7 monomers), and the sequence identities (%) of the designs from the native nsp7 were examined to comprehend the physicochemical features, the impact of mutations on nsp7 dimerization potential, and the overall stability of RdRp.<sup>32,33</sup> The superpose (CCP4: Supported Program), MayaChemTools, and ViroBLAST

packages were used to calculate RMSD, FASTA sequence of nsp7 designs, and sequence identities of all 100 000 designs against the native nsp7, respectively.

### Validation of the interface-based design and ML-based results

To assess the accuracy of our design strategy, the favourable mutations (resulting in enhanced binding affinity) obtained from Rosetta were compared with the already reported SARS-CoV-2 RdRp-nsp7 mutations reported in the CoV-GLUE database.<sup>34,35</sup> The frequency of mutations (at different min. proportion values of 0, 0.0001, 0.001, 0.01, 0.1, 0.25, 0.5, 0.75, 0.95, and 1.0) were compared with nsp7 designs to assess the precision of our design method. Heat maps were generated using the heat mapper server,<sup>36</sup> which shows the mutations at the interface and their frequencies obtained from CoV-GLUE.

To validate our ML-based predictions, an nsp7 mutant, S25L, a known stabilizer of the supercomplex, was also considered. To assess the impact of the mutation on protein stability, the MUpro server was utilized, which evaluates protein stability through three metrics:  $\Delta\Delta G$  (using a support vector machine), confidence score (using a support vector machine), and confidence score (using a neural network), where scores can range from  $-1$  to  $1$ .<sup>37</sup> In this case, a score less than zero denotes a decrease in protein stability caused by the mutation, whereas a score more than zero denotes an increase in protein stability. Scores close to  $1$  represent higher confidence in prediction.

### Mutational landscape profiles of affinity-enhancing and affinity-reducing designs

The mutational landscape profiles of the designed amino acid residues in the top-scored affinity-enhancing and affinity-reducing designs were extracted and plotted using WebLogo.<sup>38</sup> This enabled us to obtain and visually represent the types and frequencies of the nsp7-designed amino acid residues. Further, this information helped us to analyze the designed nsp7 protein mutants, their effect on stability, and the dimerization of nsp7 and RdRp.

### ML-based approaches to predict the binding affinities between the monomers in the nsp7 designs

To extrapolate trends from the CPD-generated dataset, different ML algorithms were employed. Further, to overcome the sole reliance on structural information, we leveraged ML methodologies to predict nsp7 dimer stabilizing mutations by computing the binding affinities between the nsp7 monomers. Initially, the CPD-generated dataset was utilized, and features derived from CPD—such as Rosetta total score,  $\Delta\Delta G$  (binding affinity), sequence identity, mutation positions, and mutated amino acids—were selected. Post-data preprocessing, which involved one hot encoding for converting categorical amino acid columns into numeric ones, along with data visualization and feature engineering, the dataset was split into training (80%, 80 000 data points) and test sets (20%, 20 000 data points). The  $\Delta\Delta G$  and Rosetta total scores were designated as separate target attributes for subsequent model construction. Following this,

RFR, XGBoost Regressor, and decision tree regressor were utilized to evaluate their performances. The RFR (being the top-performing algorithm in terms of accuracy as obtained in our work and assessed through the  $R^2$  score and mean absolute error) was subsequently used for model construction and further analysis. Optimal parameters for the RFR were obtained using “GridSearchCV.” To gauge the correlation between actual (CPD-derived) and predicted (ML-derived) binding affinity, the “cross\_val\_score” function was used with a CV value of 10, representing the mean of ten random cross-validation observations. The  $R^2$  score was then utilized to calculate the correlation between actual and predicted binding affinity, where a score of  $1$  signifies perfect predictions and  $0$  indicates imperfect predictions.

Here,

$$R^2 = 1 - \frac{\text{Sum squared regression (SSR)}}{\text{Total sum of squares (SST)}}$$

$$R = 1 - \frac{\sum (y_i - y_j)^2}{\sum (y_i - y_k)^2}$$

where  $y_i$  are the actual target values,  $y_j$  are the predicted target values, and  $y_k$  are the mean values of actual target values.

### ML-based approach for predicting nsp7 sequences that enhance or reduce the binding affinity between nsp7 monomers

After utilizing the CPD results to predict affinity, we adopted a reverse approach to predict nsp7 sequences that may enhance or reduce the binding affinity between the nsp7 monomers based on affinity values generated using the CPD approach. To obtain the nsp7 sequences, ‘multiclass-multioutput classification’ was utilized, which is a classification task that assigns each sample a set of non-binary properties. Thus, in this case, both the number of properties (positions) and the number of classes (sampled amino acids) per property exceed  $2$ . In the multiclass-multioutput classification model, the RFR was utilized. Given the 30 specific mutation positions for which CPD data were generated, our model encompassed 30 targets. Each target involved various classifications of amino acids that potentially serve as mutations of native residues. The input features for this prediction task were the Rosetta total score or  $\Delta\Delta G$  (binding affinity). Based on these features, mutations and eventually the nsp7 sequences at 30 different positions were predicted, thereby generating the diverse sequences.

### Intermolecular interactions between the top-scored affinity-enhancing and affinity-reducing nsp7 designs

Arpeggio and PRODIGY were utilized to calculate the intermolecular interactions between the top-scored affinity-enhancing and affinity-reducing nsp7 designs.<sup>39,40</sup> Various types of interactions and energies were obtained from this analysis, indicating how they modulate the strength and binding of the nsp7 dimers.



**Table 1** The nsp7 interface residues that are designed with corresponding SNPs of the native nsp7 sequence. A limited number of amino acids for each position were sampled in the design experiments because they are more likely to evolve naturally than the others

S. no.	Designed native nsp7 residues	Sampled SNPs in designs	S. no.	Designed native nsp7 residues	Sampled SNPs in designs
1	Ser1	ACLFPTWY	16	Ser25	ACLFPTWY
2	Lys2	RNQEIMT	17	Ser26	ACLFPTWY
3	Ser4	ACLFPTWY	18	Lys27	RNQEIMT
4	Asp5	ANEGHYV	19	Trp29	RCGLS
5	Lys7	RNQEIMT	20	Val33	ADEGILMF
6	Cys8	RGFSWY	21	His36	RNDQLPY
7	Thr9	ARNIKMPS	22	Asn37	DHIKSTY
8	Val11	ADEGILMF	23	Leu40	RQHIFPSWV
9	Val12	ADEGILMF	24	Phe49	CILSYV
10	Leu13	RQHIFPSWV	25	Glu50	ADQGKV
11	Leu14	RQHIFPSWV	26	Met52	RILKTV
12	Ser15	ACLFPTWY	27	Val53	ADEGILMF
13	Gln18	REHLKP	28	Leu56	RQHIFPSWV
14	Glu23	ADQGKV	29	Leu59	RQHIFPSWV
15	Ser24	ACLFPTWY	30	Leu60	RQHIFPSWV

adaptation of nsp7 dimer in the RdRp. For design, 30 residues of dimeric nsp7 were selected, each of which was mutated and sampled with other amino acids that naturally occur more frequently during the evolution of proteins (Table 1).

First, we analyzed the Rosetta total score vs. the RMSDs of the designs as compared to the native nsp7 dimer. It was found that, in the distribution of the Rosetta total score, RMSD ranged from 0.66 to 3.33 Å. This demonstrated that over half of the

designs retained RMSDs in the range of 1 Å to 2 Å (Fig. 2A). It was observed that, in such intricate small protein-protein complexes, acceptable structural changes can occur during the design of the 30 residues of the nsp7 and with the introduction of mutations (Fig. 2A). Here, the weighted sum of various energy terms, such as van der Waals interactions, electrostatics, and other statistical variables, is represented by the Rosetta total score. Furthermore, we conducted a control

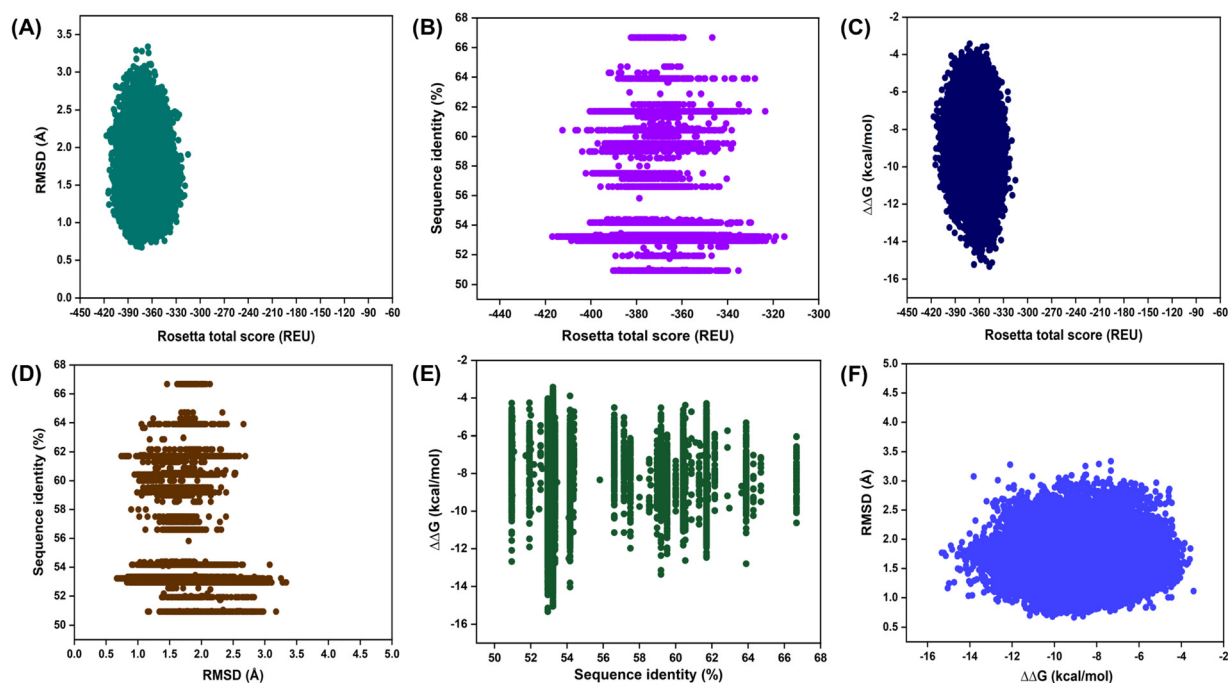


**Fig. 2** Physicochemical properties derived from the interface-based symmetrical dimer design of nsp7. (A) Rosetta total score vs. RMSD of all the obtained designs of the dimeric nsp7 is displayed. (B) Rosetta total score vs. percentage sequence identity of all the designs of the dimeric nsp7 subunit is shown. (C) Rosetta total score vs.  $\Delta\Delta G$  of all the nsp7 designs is depicted. (D) RMSD vs. percentage sequence identity of nsp7 designs is displayed. (E) Percentage sequence identity vs.  $\Delta\Delta G$  of all nsp7 designs is shown. (F)  $\Delta\Delta G$  vs. RMSD of all the nsp7 designs is displayed. Here, the designed nsp7 dimers revealed that over half of the designs maintained structural changes within the 1–2 Å RMSD range. Sequence identities ranged from 50.94% to 66.66%, and affinity-enhancing designs exhibited lower Rosetta total scores and higher binding affinities. The RMSDs of these designs correlated with both sequence identity and  $\Delta\Delta G$ , suggesting that hotspot residues are crucial. Affinity-enhancing designs predominantly displayed RMSDs between 1 and 2 Å, indicating stabilized interactions due to favourable mutations.

run where only repacking was performed on the 30 residues of nsp7. As a result, we were able to distinguish between affinity-enhancing and affinity-reducing designs. Due to the occurrence of a few unfavourable mutations, some affinity-reducing designs had RMSDs  $> 3 \text{ \AA}$  (Fig. 2A). Second, we compared the Rosetta total score with the sequence identities of all the designs. It was found that all the designs exhibited sequence identities in the range of 50.94–66.66% compared to the native nsp7 (Fig. 2B). Even though merely 25 to 30 residues were designed that form the dimeric interface, only a small number of hotspot residues were susceptible to sequence alterations (Fig. 2B).

Third, the designs were analyzed for  $\Delta\Delta G$  vs. the Rosetta total score. It was observed that the affinity-enhancing designs showed higher binding affinity and lower Rosetta total scores as compared to the affinity-reducing designs (Fig. 2C). This implies that favourable mutations positively influence the energetics, binding interface, and Rosetta total scores in the affinity-enhancing designs. Next, the RMSDs of the designs were plotted against the percentage sequence identity scores. It was found that, in the designs with the varying RMSDs from 0.66 to 3.33  $\text{\AA}$ , the percentage sequence identity also varied from 50.94% to 66.66% (Fig. 2D). Next, the  $\Delta\Delta G$  values of the generated designs were compared with their sequence identities, which indicated that designs with higher binding affinity have a relatively higher percentage sequence identity, indicating that only a few of the 30 interfacial residues designed for nsp7 are sufficient and probably the hotspot residues susceptible to mutation (Fig. 2E). Compared to the native nsp7, the CPD designs retained  $\Delta\Delta G$  in the range of  $-3.42$  to  $-15.32 \text{ kcal mol}^{-1}$  and sequence identity of 50.94% to 66.66% (Fig. 2E). Finally, we evaluated the RMSD vs.  $\Delta\Delta G$  for all the designs. We observed that the majority of the affinity-enhancing designs displayed RMSDs between 1.0 and 2.0  $\text{\AA}$ , suggesting that the associated mutations stabilized the interactions (Fig. 2F).

### Validation of the interface-based symmetrical nsp7 design approach

To examine and confirm the accuracy of our symmetric dimer design approach, a computational control analysis was carried out, where the designed mutations that enhance the binding affinity, stability, and hence the dimerization ability of the nsp7 were compared to the clinically reported nsp7 mutations of SARS-CoV-2 in the CoV-GLUE database. A comparison is conducted between the prevalence of mutations obtained from the patients and that of the nsp7 designs to reflect upon the design accuracy.

Based on the comparison, it was found that 62 out of the 235 mutations were positively selected and likely to result in stable dimers, yielding a 26.38% correlation and matching with the sequencing data (nsp7 sequences were retrieved from CoV-GLUE on 02 April 2024) (Fig. 3). Several high-frequency mutations, including K2T, V11L, and V11E, were already found to be favourable in our design computations (Fig. 3). Moreover, using the MinProp cut-off of 0.0001, one mutation out of 7 was predicted to be adaptive and positively selected to form stable nsp7 dimers in our design computations, thereby resulting in

$\sim 14.28\%$  correlation and matching with the clinically available data (Fig. S1, ESI<sup>†</sup>). As more sequencing data become available, other mutations from different populations will likely appear in addition to those sampled from our designs, thereby increasing the correlation. Therefore, this control investigation supported our design strategy and we highlighted the mutations that might serve an essential part in the adaptation and generation of high-affinity and stable nsp7 dimers.

Subsequently, we conducted a validation of our ML-based approach and its outcomes through a case study involving the S25L mutant of nsp7, known for its purported role in strengthening the RdRp–nsp7–nsp8 supercomplex. Previous studies have highlighted the significance of Ser25 and Ser26 residues in the nsp7 subunit for stabilizing the supercomplex, specifically the S25L mutation, which enhances surface complementarity by 10%, thus contributing to supercomplex stability.<sup>42</sup> Our ML-based predictions also identified an nsp7 sequence harbouring the S25L mutation, indicating potential enhanced stability for the nsp7 dimer. To independently verify this prediction, we employed the MUpPro server,<sup>37</sup> assessing protein stability through three metrics:  $\Delta\Delta G$  (support vector machine), confidence score (support vector machine), and confidence score (neural network). The results indicated  $\Delta\Delta G$  and confidence score (from SVM and neural network) to be 0.46, 0.88, and 0.83, respectively, thereby consistently supporting our ML-based prediction, and confirming that the S25L mutation augments protein stability (Table 2).

### Analysis of the mutational landscape profile and sequence variation in nsp7 dimeric designs

To gain further insights into the key differences in the types and frequencies of residues between affinity-enhancing and affinity-reducing designs, we compared the designs with each other. We analyzed the mutational landscape profiles of the designed amino acids and plotted their types and frequencies for the affinity-enhancing and affinity-reducing designs (hundred from each). The top-scored affinity-enhancing and affinity-reducing designs were analyzed based on the  $\Delta\Delta G$  values and compared for their differences in resulting mutated amino acids and hence their sequence variations (Fig. 4). This analysis showed that certain nsp7 residues such as 4(Asp5), 8(Val11), 12(Ser15), 14(Glu23), 16(Ser25), 17(Ser26), 19(Trp29), 20(Val33), 21(His36), 23(Leu40), 29(Leu59), and 30(Leu60) acquired mutations with a variety of different residues (Fig. 4). Additionally, a few residues were sampled with nearly similar residues, including those at positions 11(Leu14) and 25(Glu50) (Fig. 4). Moreover, all other residues were sampled nearly identical in both affinity-enhancing and affinity-reducing designs (Fig. 4). Through these analyses, the nsp7 hotspot residues that have the propensity to produce stable dimeric nsp7 were identified.

### ML-based approaches for predicting binding affinities between the monomers of the nsp7 designs

One of the primary objectives of this study was to employ a robust ML-based approach to predict the binding affinity between the nsp7 monomers in the dimeric nsp7 designs of

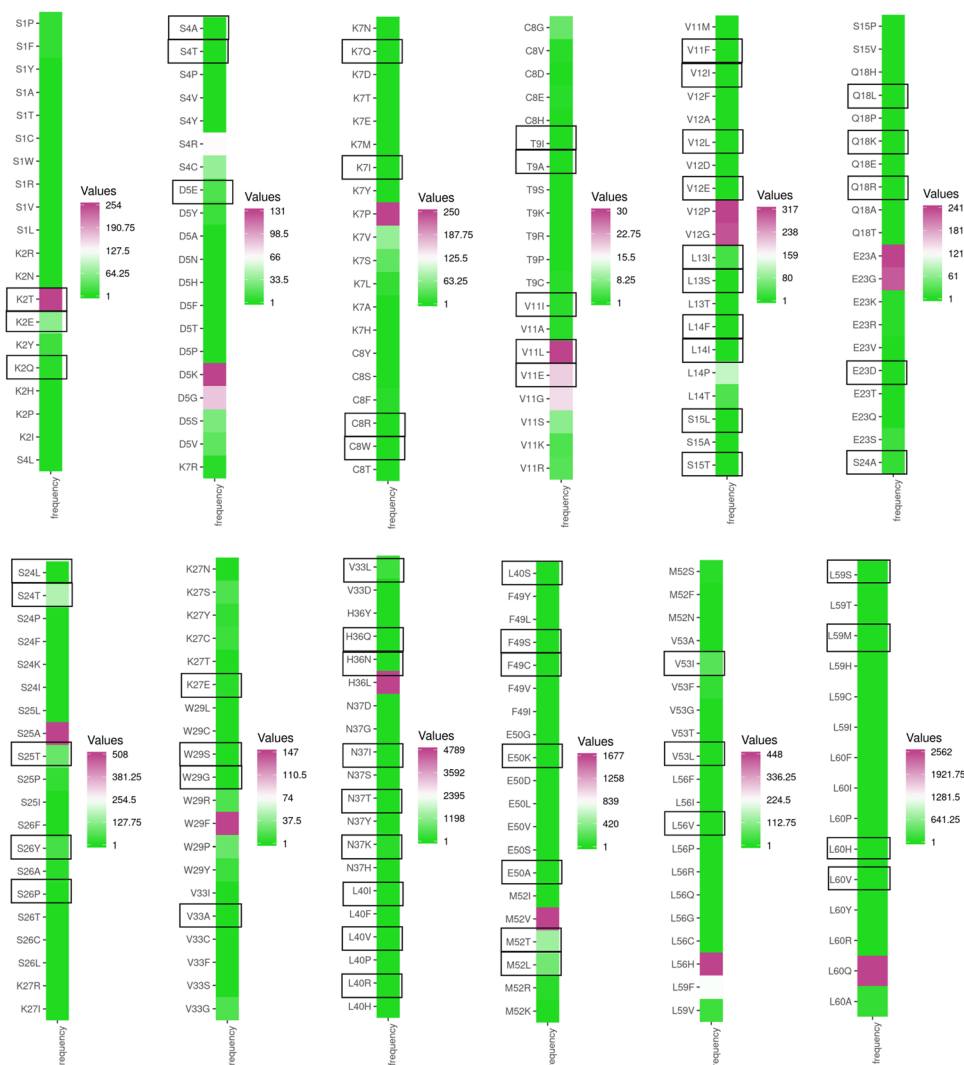


**Fig. 3** Heat map displaying nsp7 mutations and their frequencies at the dimeric nsp7 interface, derived from the CoV-GLUE database. The SARS-CoV-2 nsp7 mutations derived from the CoV-GLUE database are shown. In this illustration, the frequencies of the mutations among COVID-19 patients ranging from low to high numbers are represented using green-to-white-to-pink colours. The mutations that strengthened the dimeric nsp7 and that are derived from the CPD approach are represented with a box adjacent to the mutants. 62 mutations out of 235 were predicted to be adaptive and positively selected to form stable nsp7 dimers in our design computations, thereby resulting in ~26.38% correlation and matching with the clinically available data.

**Table 2** The effect of the S25L mutation on the stability of nsp7 protein as obtained from MUpro. The sequences are shown below and the native to mutated residues (S25 and L25) are underlined and shown in bold, respectively

S. no.	nsp7 sequence	Single point mutation	$\Delta\Delta G$ (using SVM)	Confidence score (using SVM)	Confidence score (using neural network)	Protein stability
1	SKMSDVKCTSVLLSVLQQL RVSSSKLWAQCQLHNDILLAKDTTEA FEKMSVLLSVLSM	No mutation	—	—	—	—
2	STMAEVRRASIESITVLLQLRVKT <u>LP</u> ELGAQCLQLNID IMLAKDTTEACA <u>KL</u> TL <del>SL</del> SVSMVSM	28 mutations + S25L mutation	0.46	0.88	0.83	Increase protein stability

SARS-CoV-2. This approach aimed to enhance our understanding of favourable mutations at the nsp7 dimeric interface, contributing to the stabilization of nsp7. The predictions were evaluated against CPD results, assessing their accuracy and

efficiency compared to standalone CPD methods. Among the three algorithms tested, the RFR was selected due to its superior accuracy (measured by the  $R^2$  score and mean absolute error). The analysis involved features like the Rosetta total

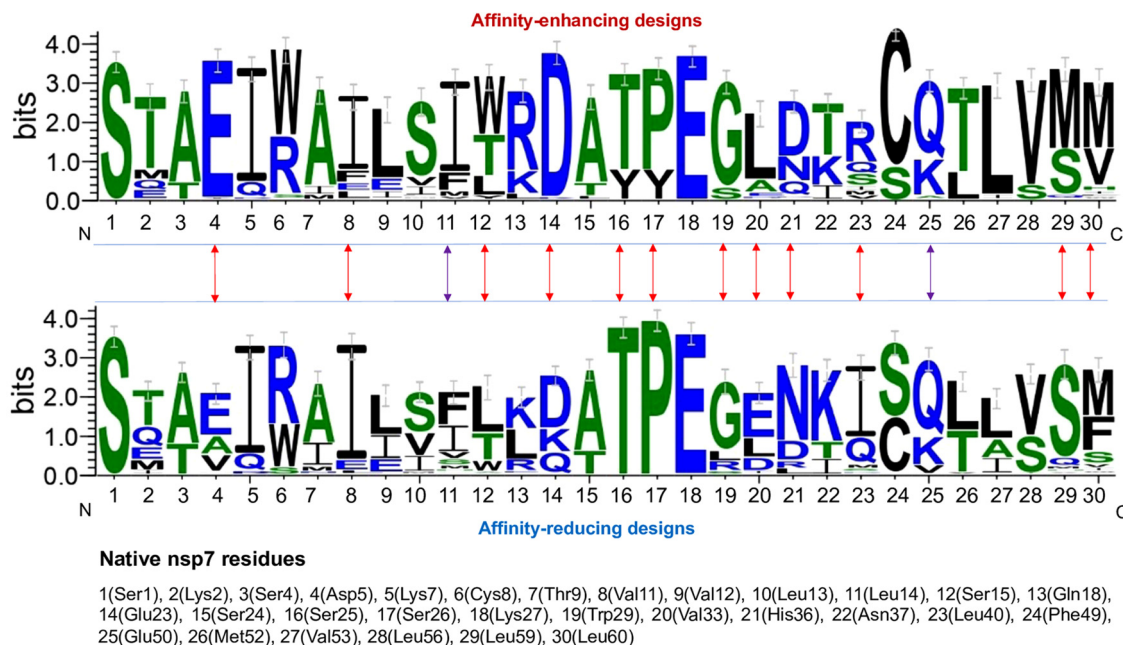


Fig. 4 Sequence logos illustrating the type and occurrence of sampled nsp7 interface residues. The sequence logo of the 100 top-scored affinity-enhancing designs and affinity-reducing nsp7 designs are shown, where native nsp7 residues are mentioned in the bottom section. In each figure, the nsp7 residues are shown on the X-axis and the Y-axis denotes the frequency of occurrence of each amino acid. The height of each symbol represents the relative frequency of a specific amino acid at the given position. The residues with diverse sequence variations between the affinity-enhancing and affinity-reducing designs are shown using red arrows and those exhibiting nearly similar residues are shown using purple arrows.

score,  $\Delta\Delta G$ , sequence identity, mutation positions, and altered amino acids. The RFR prediction model exhibited a high correlation compared to other models. In the distribution plot for the Rosetta total score and  $\Delta\Delta G$ , it was observed that the majority of designs clustered between Rosetta total scores of  $-360$  and  $-370$  REU and  $-7$  and  $-9$  kcal mol $^{-1}$   $\Delta\Delta G$ , respectively (Fig. 5A and B). The obtained  $R^2$  score of 0.80 and mean absolute error (MAE) of 3.4 between actual (CPD-derived) and predicted Rosetta total scores, along with an  $R^2$  score of 0.70 and a MAE of 0.52 between actual and predicted  $\Delta\Delta G$  with 10-fold cross-validation, highlighted the accuracy of our model (Fig. 5C and D). These findings validate the precision and reliability of our predictive model.

### ML-based sequence prediction yielding affinity-enhancing and affinity-reducing nsp7 designs

Next, to predict the nsp7 sequences harbouring mutations and to classify them as affinity-enhancing and affinity-reducing groups, an ML-based approach was utilized that relies on  $\Delta\Delta G$  (binding affinities) generated through CPD. The input for this process consisted of the Rosetta total score or  $\Delta\Delta G$ , which eventually predicted mutations at 30 distinct positions and subsequently generated the diverse nsp7 sequences (Fig. 6 and Tables S1, S2, ESI $^\dagger$ ). Our multiclass-multioutput classification model utilized an RFR. The integration of ML and CPD affirmed that affinity-enhancing designs exhibit a higher  $\Delta\Delta G$  compared to affinity-reducing designs. The predicted sequences were then juxtaposed with the native nsp7, and the resulting comparisons including  $\Delta\Delta G$ , % sequence similarity,

and RMSD of affinity-enhancing and affinity-reducing nsp7 designs were derived as shown in Tables 3 and 4.

### Interactions between the top-scored affinity-enhancing and affinity-reducing nsp7 designs

The intermolecular interactions and energetics between the top-scored affinity-enhancing and affinity-reducing nsp7 designs (as derived from CPD) were evaluated using Arpeggio and PRODIGY. In the design experiments, the affinity-enhancing design exhibited a greater number of interactions (primarily due to van der Waals interactions, hydrogen bonds, hydrophobic interactions, and proximal and carbonyl interactions) as compared to the affinity-reducing design (Table 5). Next, various types of intermolecular contacts, the number of charged and polar, apolar contacts, binding affinity, and disassociation constants were calculated between the top-scored affinity-enhancing and affinity-reducing nsp7 designs using PRODIGY. It was observed that the affinity-enhancing design retained a higher number of intermolecular interactions, a greater number of contacts such as charged-charged contacts, charged-polar contacts, charged-apolar contacts, polar-polar contacts, and therefore significantly higher binding affinity as compared to affinity-reducing design (Table 6).

Further, intermolecular contacts and binding affinity were obtained for eight different nsp7 sequences (four as affinity-enhancing and four as affinity-reducing) predicted by the ML-based approach. It was found that the affinity-enhancing designs retained a higher number of intermolecular contacts



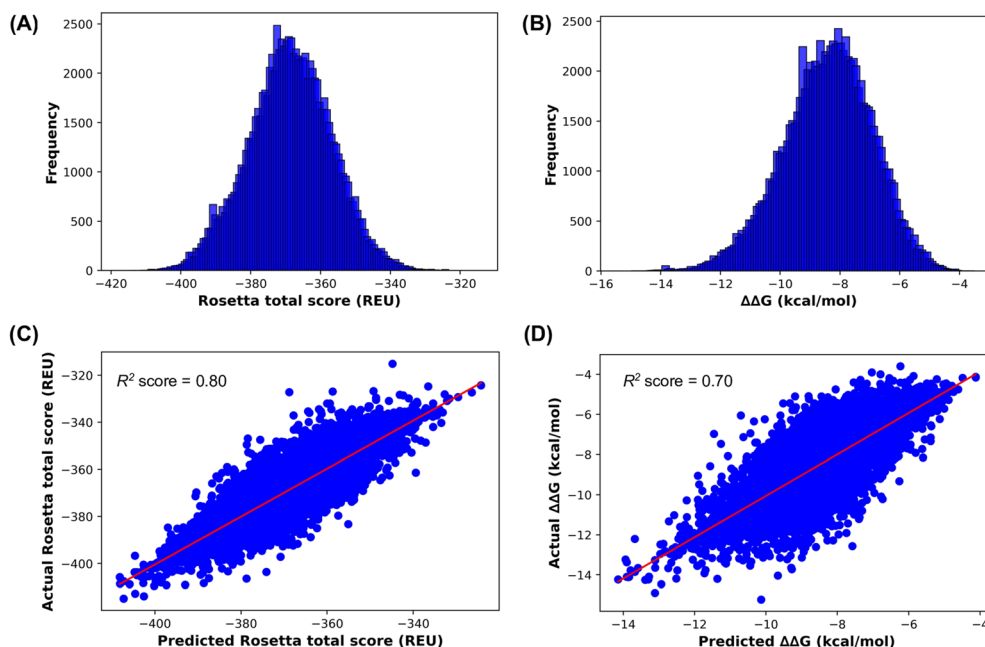


**Fig. 5** Assessment of the Rosetta total score and binding affinity correlation between CPD and ML for the nsp7 sequences. (A) and (B) Plots showing the distribution of the Rosetta total score and  $\Delta\Delta G$  with their frequency for all the CPD designs, respectively. Most designs retained the Rosetta total score centered around  $-370$  REU and  $\Delta\Delta G$  around  $-8$  kcal mol $^{-1}$ , respectively, in these distributions. (C) and (D) ML-predicted Rosetta total score vs. CPD-derived actual Rosetta total score and ML-predicted  $\Delta\Delta G$  vs. CPD-derived actual  $\Delta\Delta G$  are shown as scatter plots, respectively. A correlation coefficient of 0.80 and 0.70 (marked by a red colour line) was obtained when taking the Rosetta total score and  $\Delta\Delta G$  as targets, respectively.

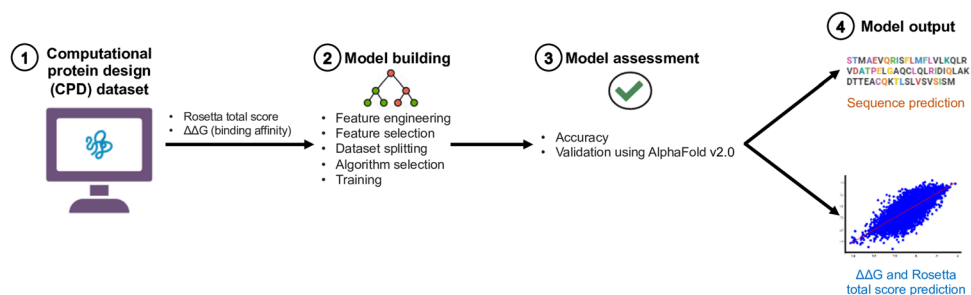


**Fig. 6** Scheme for ML-based prediction of binding affinity and newer nsp7 sequence variations. A schematic figure showing the ML-based approach and its steps that take various CPD-based features such as the Rosetta total score or  $\Delta\Delta G$  (binding affinity) as input for the model building, model assessment, and predicting the nsp7 sequences having mutations and their corresponding  $\Delta\Delta G$ .

**Table 3** ML-predicted nsp7 affinity-enhancing design sequences, their predicted  $\Delta\Delta G$ , % sequence similarity, and backbone RMSDs as compared to the native nsp7 AlphaFold v2.0 predicted structure

S. no.	ML predicted affinity-enhancing design sequences	$\Delta\Delta G$ (kcal mol $^{-1}$ )	Sequence similarity (%)	RMSD ( $\text{\AA}$ )
1	STMAEVQRISFLMFLVLKQLRVDATPELGAQCLQLRIDQLAKDTTEACQKTLISLVSISISM	-14	77.4	3.0
2	STMAEVRRASIESITVLLQLRVKTTPELGAQCLQLNIDIMLAKDTTEACAKTLISLVSVMVSM	-13	80.6	2.6
3	SQMAEVIWASFLVSLVLKQLRVDATPELGAQCDQLQKDISLAKDTTEACQKLLISLVSISISM	-13.5	77.4	4.4
4	STMAEVRRAEESSTVLRQLRVDTTPELGAQCAQLQKDIQLAKDTTEACQKTLISLVSISISM	-12.5	72.6	2.2

and various types of interactions, thereby resulting in greater binding affinity as compared to affinity-reducing designs (Tables 7 and 8). For instance, while affinity-enhancing designs had binding affinities ranging from  $-9.7$  to  $-12$  kcal mol $^{-1}$ , the

affinity-reducing designs could only show binding affinity ranging from  $-6.5$  to  $-7.7$  kcal mol $^{-1}$ , thereby demonstrating a key difference in binding affinity as a result of certain mutations in the hotspots of nsp7.

**Table 4** ML-predicted nsp7 affinity-reducing design sequences, their predicted  $\Delta\Delta G$ , % sequence similarity, and backbone RMSDs as compared to the native nsp7 AlphaFold v2.0 predicted structure

S. no.	ML predicted affinity-reducing design sequences	$\Delta\Delta G$ (kcal mol <sup>-1</sup> )	Sequence similarity (%)	RMSD (Å)
1	STMTEVIRASHISFLVLLQLRVQATPELLAQCEQLNKDIIILAKDTTEASQK LISLVSQSSM	-4	75.8	13.7
2	STMTAVIRASILVFLVLLQLRVDTTPELGAQCLQLNIDIILAKDTTEASQK LASLVSQMSM	-5	77.4	13.27
3	SQMAEVQWASFIIILVLLQLRVKATPELGAQCLQLNKDIIILAKDTTEACQ KTLSSLSSVFSM	-4.5	79.0	12.6
4	STMTEVIRISILSFLVLKQLRVDTTPELGAQCEQLNKDIVLAKDTTEASQ KTLSSLSSVMSM	-5.5	75.8	11.9

**Table 5** Intermolecular interactions obtained between the nsp7 monomers for the affinity-enhancing and affinity-reducing designs (CPD-derived) using Arpeggio

S. no.	Types of interactions	Affinity-enhancing design	Affinity-reducing design
1	van der Waals interactions	17	5
2	vdW clash interactions	14	4
3	Proximal interactions	557	350
4	Polar contacts	21	8
5	Weak polar contacts	19	9
6	Hydrogen bonds	11	2
7	Weak hydrogen bonds	12	16
8	Hydrophobic contacts	56	51
	Total number of contacts	588	359

### Structural analysis of the ML-predicted affinity-enhancing and affinity-reducing nsp7 designs

The structural evaluations of the ML-predicted affinity-enhancing and affinity-reducing nsp7 designs were performed using AlphaFold v2.0. After the model building of the sequences, the backbone RMSDs were calculated by superposing the obtained dimeric structures with the wild-type nsp7 dimeric structure. This analysis showed that the affinity-enhancing designs exhibited an optimal dimeric and symmetric nsp7 configuration with RMSDs measuring 2.2 Å, 2.6 Å, 3.0 Å, and 4.4 Å, as illustrated in Fig. 7A–D, respectively. Conversely, the affinity-reducing designs displayed higher RMSDs, ranging from 11.9 Å to 13.7 Å, as depicted in Fig. 7G–J. Notably, in an affinity-enhancing design structure, one of the nsp7 monomeric subunits demonstrated an appropriate folded structure, but failed to maintain the overall dimeric arrangement, resulting in an RMSD of 4.4 Å (Fig. 7D). Although this affinity-enhancing design displayed an RMSD of 4.4 Å, this

value pales in comparison to the affinity-reducing designs, which exhibited RMSDs ranging from 11 to 13 Å. This discrepancy underscores the relatively higher RMSD observed for the enhancing design, emphasizing its significance in our analysis. Further, most models exhibited per residue pLDDT scores exceeding 90, indicating a high level of accuracy in the affinity-enhancing models as compared to affinity-reducing models (Fig. 7E, F, K and L). These analyses substantiate the reliability and precision of our dimeric nsp7 design approach.

### Normal mode analysis of the dimeric structures of wild-type nsp7, affinity-enhancing, and affinity-reducing designs

The NMA study, utilizing internal coordinates, unveiled protein mobility, flexibility, collective motion, and potential conformational changes, aiding in assessing protein stability of the dimeric wild-type nsp7, affinity-enhancing, and affinity-reducing designs. Deformability highlights protein flexibility, with peaks indicating flexible regions like hinges. The plot comparing atom index *vs.* deformability values across normal modes for dimeric wild-type nsp7, affinity-enhancing, and affinity-reducing designs revealed heightened flexibility in the affinity-enhancing design as compared to the wild-type and affinity-reducing nsp7 designs (Fig. 8A). Next, the evaluation of the correlation covariance matrix illustrated variations for the dimeric nsp7 wild-type, as well as for the affinity-enhancing and affinity-reducing designs (Fig. 8B–D). The colours blue, white, and red were used to designate the anticorrelated, uncorrelated, and correlated states of atomic motion, respectively. The black boxes in each plot depicted the localized variation in the correlation between wild-type, affinity-enhancing, and affinity-

**Table 6** Intermolecular interactions obtained between the nsp7 monomers for the affinity-enhancing and affinity-reducing designs (CPD-derived) using PRODIGY

S. no.	Types of contacts	Affinity-enhancing design	Affinity-reducing design
1	No. of intermolecular contacts	53	38
2	No. of charged–charged contacts	6	0
3	No. of charged–polar contacts	10	2
4	No. of charged–apolar contacts	14	2
5	No. of polar–polar contacts	5	3
6	No. of apolar–polar contacts	8	9
7	No. of apolar–apolar contacts	10	22
8	Percentage of apolar NIS residues	40.00	51.92
9	Percentage of charged NIS residues	30.00	17.31
10	Predicted binding affinity (kcal mol <sup>-1</sup> )	-7.1	-5.5
11	Predicted dissociation constant (M) at 25.0 °C	$5.9 \times 10^{-6}$	$9.1 \times 10^{-5}$

**Table 7** Intermolecular contacts and predicted binding affinities obtained using PRODIGY between nsp7 monomers for the ML-predicted affinity-enhancing nsp7 designs

S. no.	Types of contacts	Affinity-enhancing design1	Affinity-enhancing design2	Affinity-enhancing design3	Affinity-enhancing design4
1	No. of intermolecular contacts	90	69	97	69
2	No. of charged–charged contacts	0	0	0	0
3	No. of charged–polar contacts	0	8	8	8
4	No. of charged–apolar contacts	8	8	16	10
5	No. of polar–polar contacts	0	7	8	0
6	No. of apolar–polar contacts	22	26	35	18
7	No. of apolar–apolar contacts	60	20	30	33
8	Percentage of apolar NIS residues	38.00	31.25	46.00	43.14
9	Percentage of charged NIS residues	24.00	31.25	24.00	23.53
10	Predicted binding affinity (kcal mol <sup>-1</sup> )	-11.3	-11.1	-12.0	-9.7
11	Predicted dissociation constant (M) at 25.0 °C	$5.0 \times 10^{-9}$	$7.0 \times 10^{-9}$	$1.6 \times 10^{-9}$	$7.5 \times 10^{-8}$

**Table 8** Intermolecular contacts and predicted binding affinities obtained using PRODIGY between nsp7 monomers for the ML-predicted affinity-reducing nsp7 designs

S. no.	Types of contacts	Affinity-reducing design1	Affinity-reducing design2	Affinity-reducing design3	Affinity-reducing design4
1	No. of intermolecular contacts	39	52	46	47
2	No. of charged–charged contacts	1	0	0	2
3	No. of charged–polar contacts	4	2	2	0
4	No. of charged–apolar contacts	4	8	9	6
5	No. of polar–polar contacts	2	7	0	3
6	No. of apolar–polar contacts	9	15	9	12
7	No. of apolar–apolar contacts	19	20	26	24
8	Percentage of apolar NIS residues	49.07	44.44	52.73	45.63
9	Percentage of charged NIS residues	17.59	20.37	16.36	27.18
10	Predicted binding affinity (kcal mol <sup>-1</sup> )	-6.5	-7.7	-6.8	-6.6
11	Predicted dissociation constant (M) at 25.0 °C	$1.7 \times 10^{-5}$	$2.4 \times 10^{-6}$	$1.1 \times 10^{-5}$	$1.5 \times 10^{-5}$

reducing designs (Fig. 8B–D). Finally, the eigenvalue analysis demonstrated significantly higher eigenvalues in the affinity-enhancing design, suggesting enhanced localized motions such as side-chain vibrations, as compared to the dimeric wild-type nsp7 and affinity-reducing designs (Fig. S2, ESI†).

## Discussion

The ongoing COVID-19 pandemic, caused by SARS-CoV-2, underscores the need for comprehensive insights into the components and life cycle of the virus.<sup>43</sup> SARS-CoV-2, a positive-sense, single-stranded RNA virus, exhibits genetic variability, resulting in the development of variants with potential implications for transmissibility, severity, and vaccine efficacy.<sup>44</sup> Understanding the molecular mechanisms underlying viral replication, immune evasion, and pathogenesis is crucial, particularly regarding the roles of the intracellular proteins in the lifecycle of the virus.<sup>45</sup> The RdRp, a central player in viral replication, catalyzes the synthesis of negative-sense RNA strands crucial for the survival of the virus.<sup>46</sup> While the standalone RdRp exhibits minimal activity due to nsp12, the incorporation of its cofactors, nsp7 and nsp8, significantly amplifies its polymerase activity.<sup>47,48</sup> Although different viral nsp subunits play a role in the replication and transcription

processes, the nsp12–nsp7–nsp8 complex serves as the minimal configuration essential for nucleotide polymerization.<sup>19</sup> The dimerization of RdRp *via* the nsp subunits, notably nsp7, is essential for its functionality, governing viral RNA copying efficiency. The antiparallel arrangement of the RdRp dimer reveals the interaction of the two polymerases through nsp7 subunits, facilitated by the  $\alpha 1$  and  $\alpha 3$  helices (residues 2–20 and 44–62). Dissociation of nsp8b exposes the dimerization region of nsp7, enabling the formation of an nsp7–nsp7 dimer interface. Previous studies have indicated that mutations in RdRp subunits can impact the stability of both monomers and dimers.<sup>20</sup> Therefore, investigating RdRp dimerization mechanisms could offer insights into potential antiviral strategies and therapeutic targets.

In some of our previous studies, we implemented high-throughput protein design methodologies to figure out critical residues and mutations within the intracellular proteins of SARS-CoV-2, including RdRp,<sup>33</sup> main protease (M<sup>pro</sup>),<sup>32</sup> and spike protein RBD,<sup>26</sup> impacting the adaptability of the virus to antiviral drugs and antibody therapeutics. This study delved into the design and analysis of nsp7 mutations that may have an impact on the stability, adaptation, and fitness of nsp7 dimers. This comprehensive approach involved an integration of high-throughput symmetrical protein design, ML, structural analysis, and validation of the computational predictions using

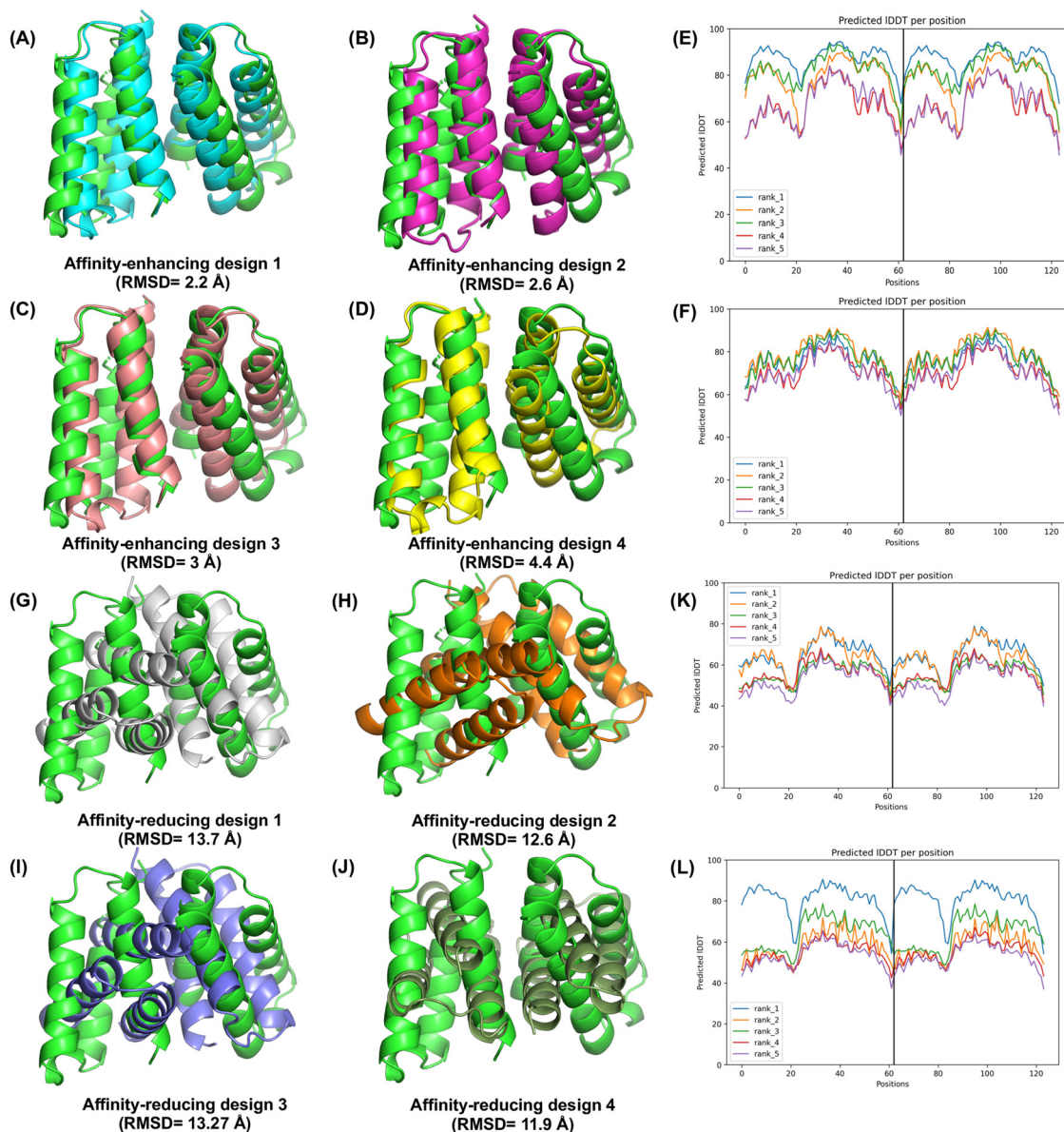
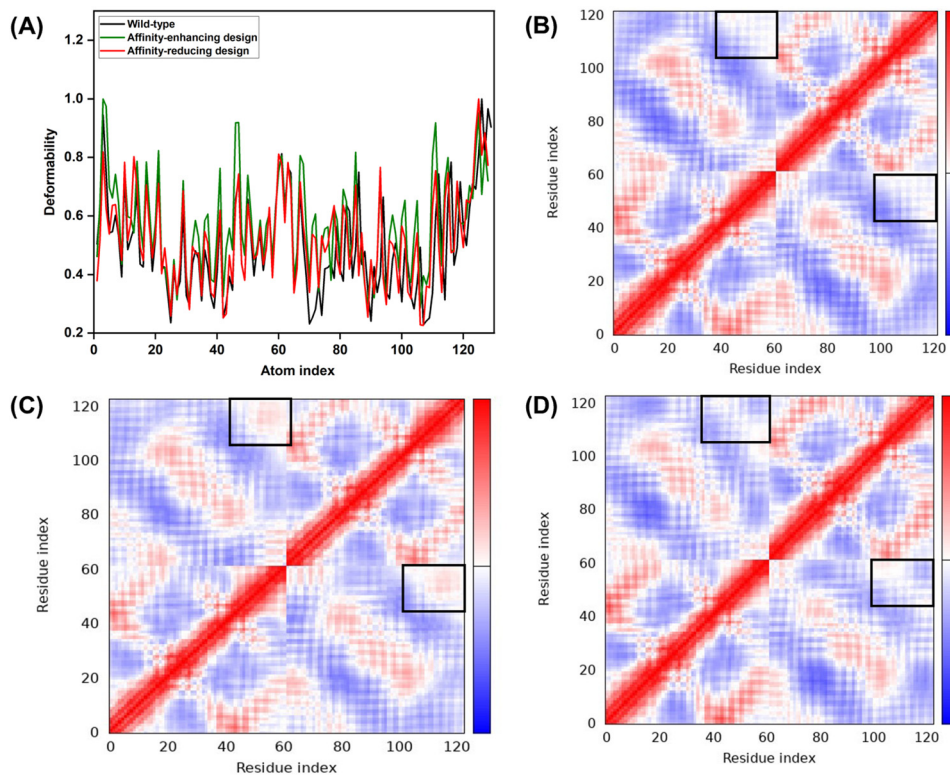


Fig. 7 Structure prediction and modeling of the affinity-enhancing and affinity-reducing nsp7 designs using AlphaFold v2.0. In (A)–(D) and (G)–(J), AlphaFold v2.0 derived structures of the affinity-enhancing and affinity-reducing nsp7 designs along with their backbone RMSDs when superposed with native nsp7 dimer are presented, respectively. In (E), (F), (K) and (L), the predicted LDDT (pLDDT) of the top-ranked models for the affinity-enhancing and affinity-reducing designs are displayed, respectively, to assess the quality of the models.

an array of strategies (Fig. 3). The electron microscopic structure of the RdRp complex utilized by the CPD approach guided the identification of potential hotspot residues within the dimeric nsp7 interface (Fig. 1). Symmetrical protein design using Rosetta aimed to modulate the dimerization of nsp7, considering 30 selected residues (Table 1). The results demonstrated acceptable structural changes, emphasizing the intricate nature of small protein–protein complexes. Several features, including the Rosetta total score, RMSD, and sequence identity, were analyzed to assess the designs, their physicochemical properties, and mutational landscape profiles (Fig. 2 and 4). Affinity-enhancing designs exhibited favourable energetics, lower Rosetta total scores, and higher binding

affinity compared to affinity-reducing counterparts. Subsequently, ML-predicted results correlated well with the CPD results and provided additional insights. The RFR model outperformed other algorithms, showcasing its accuracy in predicting binding affinities (Fig. 5). ML-based sequence prediction further elucidated the potential nsp7 sequences harbouring mutations (indicating affinity-enhancing and affinity-reducing classifications), providing insights into their binding affinity, Rosetta total score, and capability to derive new sequence combinations (Fig. 6 and Tables 7, 8). The AlphaFold v2.0 structural analysis provided insights into the optimal dimeric configurations of affinity-enhancing designs, further validating the precision of our approach presented here



**Fig. 8** Results obtained from the NMA-based analysis of the dimeric structures of wild-type nsp7, affinity-enhancing, and affinity-reducing designs. Panel (A) presents the deformability plot, depicting the atom index vs. deformability scores across normal modes for the dimeric structures of nsp7 wild-type, as well as for the affinity-enhanced and affinity-reducing designs conducted using iMODS. Panels (B)–(D) display the covariance matrix for the dimeric nsp7 wild-type, affinity-enhancing, and affinity-reducing designs, with red, white, and blue colours indicating correlated, uncorrelated, and anti-correlated motions, respectively. The black boxes in each plot in panels (B)–(D) illustrate the localized differences in correlation among the wild-type, affinity-enhancing, and affinity-reducing designs.

(Fig. 7). Employing NMA-based analysis, our study further provided insights into the protein dynamics and stability of the dimeric structures of wild-type nsp7, affinity-enhancing, and affinity-reducing designs. Deformability plots highlighted the flexible regions, with affinity-enhancing designs showing increased flexibility (Fig. 8A). Correlation covariance matrices revealed distinct atomic motion states (Fig. 8B–D). Eigenvalue analysis indicated localized motions, emphasizing differences between the dimeric wild-type nsp7, and the affinity-enhancing and affinity-reducing designs (Fig. S2, ESI†). Finally, our comprehensive study not only provided valuable insights into the mechanisms governing nsp7 affinity-enhancing and affinity-reducing designs but also contributed to the understanding of the dynamic nature of viral mutations and their impact on viral fitness. The revealed physicochemical properties, molecular interactions, and sequence predictions of the dimeric nsp7 subunit may offer potential avenues for therapeutic intervention in combating COVID-19.

## Limitations of the study

The study has certain limitations. Firstly, the complexity of the Rosetta symmetrical dimeric interface design script constrained our ability to carry out a symmetric design of all

subunits of the RdRp. Specifically, only the nsp7 subunit was designed, necessitating the development of an advanced symmetrical dimeric interface protocol to encompass all RdRp subunits for a more comprehensive assessment of mutation effects. Secondly, while CPD- and ML-based approaches successfully predicted favourable mutations on the dimeric nsp7 interface, experimental validation is indispensable to ascertain the actual binding affinity between the designed nsp7 monomers. Thirdly, other robust computational approaches could be utilized to obtain single-point mutations of nsp7 that may drive the sequences towards a stronger or weaker binding between the nsp7 monomers. However, to address these limitations and validate the precision of our approach, we cross-referenced our predictions with clinically known mutations in the SARS-CoV-2 nsp7 subunit of RdRp. These mutations, known in clinical contexts, provide additional evidence supporting the adaptability and stability of nsp7 dimers.

## Conclusion

In conclusion, our study addresses the critical aspects of SARS-CoV-2 intracellular proteins, exploring the intricate dynamics of its RdRp, particularly the nsp7 subunit. Concerning the COVID-19 pandemic, understanding the molecular intricacies of viral

components becomes paramount. Our research employs a comprehensive approach, shedding light on the stability, adaptation, and fitness of nsp7 dimers. The study reveals that nsp7, a crucial player in viral replication, forms symmetrical dimers through a complex interface, influencing binding affinity and stability. By employing a Rosetta-based design strategy and ML-based predictions, we identified specific hotspot residues within the dimeric nsp7 interface. Affinity-enhancing designs exhibited favourable energetics and higher binding affinity, validated through structural analyses using AlphaFold v2.0. Importantly, our predictions align with clinically known mutations, providing real-world validation. While our focus on the nsp7 subunit offers substantial insights, acknowledging the necessity for a comprehensive analysis involving all RdRp subunits becomes crucial. In the broader context, our findings contribute valuable information for potential therapeutic interventions against COVID-19, emphasizing the dynamic nature of viral mutations and their impact on viral fitness.

## Author contributions

Amar Jeet Yadav, Shivank Kumar, Shweeta Maurya, Khushboo Bhagat, and Aditya K. Padhi contributed to the conceptualization, formal analysis, investigation, methodology, and writing of the original draft. Aditya K. Padhi contributed to conceptualization. Aditya K. Padhi contributed to funding acquisition and project administration. All authors contributed to the writing and preparation of the final version of the manuscript.

## Conflicts of interest

There are no conflicts to declare.

## Acknowledgements

The authors sincerely acknowledge the infrastructure facilities of IIT (BHU) Varanasi and DST-funded I-DAPT Hub Foundation, IIT (BHU) [DST/NMICPS/TIH11/IIT(BHU)2020/02]. Further, the computing resources of PARAM Shivay Facility under the National Supercomputing Mission, Government of India at the IIT (BHU), Varanasi, are gratefully acknowledged. A. J. Y., S. M., and K. B. acknowledge the Ministry of Human Resource Development (MHRD), the Government of India, and IIT (BHU) for their research fellowships. A. K. P. is grateful for the financial support received from the Science & Engineering Research Board (SERB), Government of India's Project No. SRG/2023/000167 and Indian Institute of Technology (Banaras Hindu University) Varanasi's Seed Grant ref. No. IIT (BHU)/Budget/19-(14)/2022-23/17507.

## References

- 1 P. V. Markov, M. Ghafari, M. Beer, K. Lythgoe, P. Simmonds, N. I. Stilianakis and A. Katzourakis, The evolution of SARS-CoV-2, *Nat. Rev. Microbiol.*, 2023, **21**, 361–379.
- 2 A. Sharma, S. Tiwari, M. K. Deb and J. L. Marty, Severe acute respiratory syndrome coronavirus-2 (SARS-CoV-2): a global pandemic and treatment strategies, *Int. J. Antimicrob. Agents*, 2020, **56**, 106054.
- 3 A. A. T. Naqvi, K. Fatima, T. Mohammad, U. Fatima, I. K. Singh, A. Singh, S. M. Atif, G. Hariprasad, G. M. Hasan and Md. I. Hassan, Insights into SARS-CoV-2 genome, structure, evolution, pathogenesis and therapies: structural genomics approach, *Biochim. Biophys. Acta, Mol. Basis Dis.*, 2020, **1866**, 165878.
- 4 H. Yang and Z. Rao, Structural biology of SARS-CoV-2 and implications for therapeutic development, *Nat. Rev. Microbiol.*, 2021, **19**, 685–700.
- 5 R. Yadav, J. K. Chaudhary, N. Jain, P. K. Chaudhary, S. Khanra, P. Dhamija, A. Sharma, A. Kumar and S. Handu, Role of Structural and Non-Structural Proteins and Therapeutic Targets of SARS-CoV-2 for COVID-19, *Cells*, 2021, **10**, 821.
- 6 C. B. Jackson, M. Farzan, B. Chen and H. Choe, Mechanisms of SARS-CoV-2 entry into cells, *Nat. Rev. Mol. Cell Biol.*, 2022, **23**, 3–20.
- 7 P. V'kovski, A. Kratzel, S. Steiner, H. Stalder and V. Thiel, Coronavirus biology and replication: implications for SARS-CoV-2, *Nat. Rev. Microbiol.*, 2021, **19**, 155–170.
- 8 Z. Almubaid and H. Al-Mubaid, Analysis and comparison of genetic variants and mutations of the novel coronavirus SARS-CoV-2, *Gene Rep*, 2021, **23**, 101064.
- 9 A. A. Rabaan, S. H. Al-Ahmed, H. Albayat, S. Alwarthan, M. Alhajri, M. A. Najim, B. M. AlShehail, W. Al-Adsani, A. Alghadeer, W. A. Abduljabbar, N. Alotaibi, J. Alsalman, A. H. Gorab, R. S. Almaghrabi, A. A. Zaidan, S. Aldossary, M. Alissa, L. M. Alburaiqy, F. M. Alsalim, N. Thakur, G. Verma and M. Dhawan, Variants of SARS-CoV-2: Influences on the Vaccines' Effectiveness and Possible Strategies to Overcome Their Consequences, *Medicina (B Aires)*, 2023, **59**, 507.
- 10 A. M. Carabelli, T. P. Peacock, L. G. Thorne, W. T. Harvey, J. Hughes, T. I. de Silva, S. J. Peacock, W. S. Barclay, T. I. de Silva, G. J. Towers and D. L. Robertson, SARS-CoV-2 variant biology: immune escape, transmission and fitness, *Nat. Rev. Microbiol.*, 2023, **21**, 162–177.
- 11 J. K. Das, B. Thakuri, K. MohanKumar, S. Roy, A. Sljoka, G.-Q. Sun and A. Chakraborty, Mutation-Induced Long-Range Allosteric Interactions in the Spike Protein Determine the Infectivity of SARS-CoV-2 Emerging Variants, *ACS Omega*, 2021, **6**, 31305–31320.
- 12 Q. Zhang, R. Xiang, S. Huo, Y. Zhou, S. Jiang, Q. Wang and F. Yu, Molecular mechanism of interaction between SARS-CoV-2 and host cells and interventional therapy, *Signal Transduction Targeted Ther.*, 2021, **6**, 233.
- 13 W. Wu, Y. Cheng, H. Zhou, C. Sun and S. Zhang, The SARS-CoV-2 nucleocapsid protein: its role in the viral life cycle, structure and functions, and use as a potential target in the development of vaccines and diagnostics, *Virol. J.*, 2023, **20**, 6.
- 14 Y. Jiang, W. Yin and H. E. Xu, RNA-dependent RNA polymerase: structure, mechanism, and drug discovery for

- COVID-19, *Biochem. Biophys. Res. Commun.*, 2021, **538**, 47–53.
- 15 A. J. W. te Velthuis, J. M. Grimes and E. Fodor, Structural insights into RNA polymerases of negative-sense RNA viruses, *Nat. Rev. Microbiol.*, 2021, **19**, 303–318.
  - 16 X. Yin, H. Popa, A. Stapon, E. Bouda and M. Garcia-Diaz, Fidelity of Ribonucleotide Incorporation by the SARS-CoV-2 Replication Complex, *J. Mol. Biol.*, 2023, **435**, 167973.
  - 17 E. J. Snijder, E. Decroly and J. Ziebuhr, The Nonstructural Proteins Directing Coronavirus RNA Synthesis and Processing, *Adv. Virus Res.*, 2016, **96**, 59–126.
  - 18 E. Konkolova, M. Klima, R. Nencka and E. Boura, Structural analysis of the putative SARS-CoV-2 primase complex, *J. Struct. Biol.*, 2020, **211**, 107548.
  - 19 R. N. Kirchdoerfer and A. B. Ward, Structure of the SARS-CoV nsp12 polymerase bound to nsp7 and nsp8 co-factors, *Nat. Commun.*, 2019, **10**, 2342.
  - 20 F. A. Jochheim, D. Tegunov, H. S. Hillen, J. Schmitzová, G. Kokic, C. Dienemann and P. Cramer, The structure of a dimeric form of SARS-CoV-2 polymerase, *Commun. Biol.*, 2021, **4**, 999.
  - 21 A. K. Padhi and T. Tripathi, A comprehensive protein design protocol to identify resistance mutations and signatures of adaptation in pathogens, *Brief Funct. Genomics*, 2023, **22**, 195–203.
  - 22 P. Kalita, T. Tripathi and A. K. Padhi, Computational Protein Design for COVID-19 Research and Emerging Therapeutics, *ACS Cent. Sci.*, 2023, **9**, 602–613.
  - 23 A. K. Padhi, R. Shukla, P. Saudagar and T. Tripathi, High-throughput rational design of the remdesivir binding site in the RdRp of SARS-CoV-2: implications for potential resistance, *iScience*, 2021, **24**, 101992.
  - 24 F. Kabinger, C. Stiller, J. Schmitzová, C. Dienemann, G. Kokic, H. S. Hillen, C. Höbartner and P. Cramer, Mechanism of molnupiravir-induced SARS-CoV-2 mutagenesis, *Nat. Struct. Mol. Biol.*, 2021, **28**, 740–746.
  - 25 A. K. Padhi and T. Tripathi, Hotspot residues and resistance mutations in the nirmatrelvir-binding site of SARS-CoV-2 main protease: design, identification, and correlation with globally circulating viral genomes, *Biochem. Biophys. Res. Commun.*, 2022, **629**, 54–60.
  - 26 S. Maurya, S. Kumar and A. K. Padhi, Interface-Guided Computational Protein Design Reveals Bebtelovimab-Resistance Mutations in SARS-CoV-2 RBD: Correlation with Global Viral Genomes and Bebtelovimab-Escape Mutations, *ChemistrySelect*, 2023, **8**(46), e20230290.
  - 27 K. K. Yang, Z. Wu and F. H. Arnold, Machine-learning-guided directed evolution for protein engineering, *Nat. Methods*, 2019, **16**, 687–694.
  - 28 J. Jumper, R. Evans, A. Pritzel, T. Green, M. Figurnov, O. Ronneberger, K. Tunyasuvunakool, R. Bates, A. Židek, A. Potapenko, A. Bridgland, C. Meyer, S. A. A. Kohl, A. J. Ballard, A. Cowie, B. Romera-Paredes, S. Nikolov, R. Jain, J. Adler, T. Back, S. Petersen, D. Reiman, E. Clancy, M. Zielinski, M. Steinegger, M. Pacholska, T. Berghammer, S. Bodenstein, D. Silver, O. Vinyals, A. W. Senior, K. Kavukcuoglu, P. Kohli and D. Hassabis, Highly accurate protein structure prediction with AlphaFold, *Nature*, 2021, **596**, 583–589.
  - 29 R. F. Alford, A. Leaver-Fay, J. R. Jeliazkov, M. J. O'Meara, F. P. DiMaio, H. Park, M. V. Shapovalov, P. D. Renfrew, V. K. Mulligan, K. Kappel, J. W. Labonte, M. S. Pacella, R. Bonneau, P. Bradley, R. L. Dunbrack, R. Das, D. Baker, B. Kuhlman, T. Kortemme and J. J. Gray, The Rosetta All-Atom Energy Function for Macromolecular Modeling and Design, *J. Chem. Theory Comput.*, 2017, **13**, 3031–3048.
  - 30 S. J. Fleishman, A. Leaver-Fay, J. E. Corn, E.-M. Strauch, S. D. Khare, N. Koga, J. Ashworth, P. Murphy, F. Richter, G. Lemmon, J. Meiler and D. Baker, RosettaScripts: A Scripting Language Interface to the Rosetta Macromolecular Modeling Suite, *PLoS One*, 2011, **6**, e20161.
  - 31 P. B. Stranges, M. Machius, M. J. Miley, A. Tripathy and B. Kuhlman, Computational design of a symmetric homodimer using  $\beta$ -strand assembly, *Proc. Natl. Acad. Sci. U. S. A.*, 2011, **108**, 20562–20567.
  - 32 A. K. Padhi and T. Tripathi, High-throughput design of symmetrical dimeric SARS-CoV-2 main protease: structural and physical insights into hotspots for adaptation and therapeutics, *Phys. Chem. Chem. Phys.*, 2022, **24**, 9141–9145.
  - 33 A. K. Padhi, J. Dandapat, P. Saudagar, V. N. Uversky and T. Tripathi, Interface-based design of the favipiravir-binding site in SARS-CoV-2 RNA-dependent RNA polymerase reveals mutations conferring resistance to chain termination, *FEBS Lett.*, 2021, **595**, 2366–2382.
  - 34 S. Elbe and G. Buckland-Merrett, Data, disease and diplomacy: GISAID's innovative contribution to global health, *Global Challenges*, 2017, **1**, 33–46.
  - 35 G. R. C. M. R. D. Singer J, CoV-GLUE: a web application for tracking SARS-CoV-2 genomic variation, Preprints (Basel).
  - 36 S. Babicki, D. Arndt, A. Marcu, Y. Liang, J. R. Grant, A. Maciejewski and D. S. Wishart, Heatmapper: web-enabled heat mapping for all, *Nucleic Acids Res.*, 2016, **44**, W147–W153.
  - 37 J. Cheng, A. Randall and P. Baldi, Prediction of protein stability changes for single-site mutations using support vector machines, *Proteins: Struct., Funct., Bioinf.*, 2006, **62**, 1125–1132.
  - 38 G. E. Crooks, G. Hon, J.-M. Chandonia and S. E. Brenner, WebLogo: A Sequence Logo Generator: Fig. 1, *Genome Res.*, 2004, **14**, 1188–1190.
  - 39 H. C. Jubb, A. P. Higuero, B. Ochoa-Montaña, W. R. Pitt, D. B. Ascher and T. L. Blundell, Arpeggio: A Web Server for Calculating and Visualising Interatomic Interactions in Protein Structures, *J. Mol. Biol.*, 2017, **429**, 365–371.
  - 40 L. C. Xue, J. P. Rodrigues, P. L. Kastiris, A. M. Bonvin and A. Vangone, PRODIGY: a web server for predicting the binding affinity of protein–protein complexes, *Bioinformatics*, 2016, **32**, 3676–3678.
  - 41 J. R. López-Blanco, J. I. Aliaga, E. S. Quintana-Ortí and P. Chacón, iMODS: internal coordinates normal mode analysis server, *Nucleic Acids Res.*, 2014, **42**, W271–W276.
  - 42 S. M. S. Reshamwala, V. Likhite, M. S. Degani, S. S. Deb and S. B. Noronha, Mutations in SARS-CoV-2 nsp7 and nsp8

- proteins and their predicted impact on replication/transcription complex structure, *J. Med. Virol.*, 2021, **93**, 4616–4619.
- 43 I. P. Trougakos, K. Stamatelopoulos, E. Terpos, O. E. Tsitsilonis, E. Aivalioti, D. Paraskevis, E. Kastritis, G. N. Pavlakis and M. A. Dimopoulos, Insights to SARS-CoV-2 life cycle, pathophysiology, and rationalized treatments that target COVID-19 clinical complications, *J. Biomed. Sci.*, 2021, **28**, 9.
- 44 A. Dubey, S. Choudhary, P. Kumar and S. Tomar, Emerging SARS-CoV-2 Variants: Genetic Variability and Clinical Implications, *Curr. Microbiol.*, 2021, **79**, 20.
- 45 T. Nelemans and M. Kikkert, Viral Innate Immune Evasion and the Pathogenesis of Emerging RNA Virus Infections, *Viruses*, 2019, **11**, 961.
- 46 S. Venkataraman, B. V. L. S. Prasad and R. Selvarajan, RNA Dependent RNA Polymerases: Insights from Structure, Function and Evolution, *Viruses*, 2018, **10**, 76.
- 47 Q. Peng, R. Peng, B. Yuan, J. Zhao, M. Wang, X. Wang, Q. Wang, Y. Sun, Z. Fan, J. Qi, G. F. Gao and Y. Shi, Structural and Biochemical Characterization of the nsp12–nsp7–nsp8 Core Polymerase Complex from SARS-CoV-2, *Cell Rep.*, 2020, **31**, 107774.
- 48 L. Subissi, C. C. Posthuma, A. Collet, J. C. Zevenhoven-Dobbe, A. E. Gorbalenya, E. Decroly, E. J. Snijder, B. Canard and I. Imbert, One severe acute respiratory syndrome coronavirus protein complex integrates processive RNA polymerase and exonuclease activities, *Proc. Natl. Acad. Sci. U. S. A.*, 2014, **111**(37), E3900–9.